



# Reversible loss of core-shell structure for Ni-Au bimetallic nanoparticles during CO<sub>2</sub> hydrogenation

Xiaoben Zhang<sup>1,2,9</sup>, Shaobo Han<sup>3,9</sup>, Beien Zhu<sup>4,5,9</sup>, Guanghui Zhang<sup>6,7,9</sup>, Xiaoyan Li<sup>2,5</sup>, Yi Gao<sup>4,5</sup>✉, Zhaoxuan Wu<sup>1</sup>, Bing Yang<sup>1</sup>✉, Yuefeng Liu<sup>1</sup>, Walid Baaziz<sup>8</sup>, Ovidiu Ersen<sup>8</sup>, Meng Gu<sup>3</sup>✉, Jeffrey T. Miller<sup>7</sup> and Wei Liu<sup>1</sup>✉

**The high catalytic performance of core-shell nanoparticles is usually attributed to their distinct geometric and electronic structures. Here we reveal a dynamic mechanism that overturns this conventional understanding by a direct environmental transmission electron microscopy visualization coupled with multiple state-of-the-art in situ techniques, which include synchrotron X-ray absorption spectroscopy, infrared spectroscopy and theoretical simulations. A Ni-Au catalytic system, which exhibits a highly selective CO production in CO<sub>2</sub> hydrogenation, features an intact ultrathin Au shell over the Ni core before and after the reaction. However, the catalytic performance could not be attributed to the Au shell surface, but rather to the formation of a transient reconstructed alloy surface, promoted by CO adsorption during the reaction. The discovery of such a reversible transformation urges us to reconsider the reaction mechanism beyond the stationary model, and may have important implications not only for core-shell nanoparticles, but also for other well-defined nanocatalysts.**

Catalyst design faces serious challenges, because even a well-designed catalyst can unpredictably change its size, structure and active surface composition during reactions to yield functional results that do not match the predictions based on static characterizations<sup>1–5</sup>. Bimetallic core-shell catalysts have attracted tremendous interest for a variety of heterogeneous and electrochemical reactions, and an extraordinary catalytic performance. It is accepted that their catalytic properties are determined by the synergy of the electronic and geometric features that originate at the interface between the core and the top shell layer<sup>6</sup>. Reducing the shell thickness to a few atomic layers can maximize the lattice strain<sup>7,8</sup> and the electronic effects<sup>9</sup> on the outer surface of the bimetallic particles, which is believed to enhance the catalytic performance and reduce the consumption of precious metals. However, this explanation only holds true if the intact core-shell retains its distinctive structure during the entire reaction. Although some pioneering works report on the reaction-induced and/or thermally induced surface segregation processes during the reaction<sup>10–15</sup>, it was not clear whether a core-shell nanoparticle (NP) maintains its structure throughout a reaction. Most studies on core-shell nanocatalysts are primarily established based on the catalyst's static structures before and/or after a reaction<sup>16</sup>.

In this work, we report a different working mechanism and demonstrate that the core-shell structure may not exist under a specific set of conditions. By using environmental transmission electron microscopy (ETEM) to directly visualize the dynamic process at atomic level, we saw a core-shell Ni@Au that kinetically

transformed into a NiAu alloy during the CO<sub>2</sub> hydrogenation and fully reversed back to its previous core-shell configuration after the reaction. By precisely analysing the imaging conditions of over 3,000 high-resolution transmission electron microscopy (TEM) images, we were able to trace the real-time changes of the surface atomic structure during the entire reaction process, under reaction pressures that ranged from several pascals to one atmosphere. The microscopy discovery is well supported by in situ Fourier transform infrared (FTIR) spectroscopy and in situ synchrotron X-ray absorption spectroscopy (XAS). Density functional theory (DFT) calculations also confirmed that it is the kinetically alloyed surface, rather than the ultrathin Au shell surface, that is catalytically active during the highly selective reverse water gas shift reaction.

## Results

**Atomic structure and CO<sub>2</sub> hydrogenation performance characterized under static conditions.** NiAu bimetallic NPs were prepared using a wet chemical method<sup>17</sup>, and further supported on silica with a loading of 1.33 wt% Au and 3.83 wt% Ni (Supplementary Table 1). The high angle annular dark field scanning transmission electron microscopy (HAADF-STEM) images in Fig. 1a,b show that the NiAu catalyst maintained the core-shell structure before and after the reaction, and the particle sizes slightly increased (Supplementary Fig. 1). An atomically resolved HAADF-STEM image (Fig. 1c) and an X-ray energy dispersion spectroscopy measurements (Fig. 1d) further reveal the typical structure of a core-shell NP, which consists of a face-centred cubic Ni core, and 2–3 atomic layers of an

<sup>1</sup>Dalian National Laboratory for Clean Energy, Dalian Institute of Chemical Physics (DICP), Chinese Academy of Sciences, Dalian, China. <sup>2</sup>University of Chinese Academy of Sciences, Beijing, China. <sup>3</sup>Department of Materials Science and Engineering, Southern University of Science and Technology, Shenzhen, China. <sup>4</sup>Zhangjiang Laboratory, Shanghai Advanced Research Institute, Chinese Academy of Sciences, Shanghai, China. <sup>5</sup>Division of Interfacial Water and Key Laboratory of Interfacial Physics and Technology, Shanghai Institute of Applied Physics, Chinese Academy of Sciences, Shanghai, China. <sup>6</sup>State Key Laboratory of Fine Chemicals, PSU-DUT Joint Center for Energy Research, School of Chemical Engineering, Dalian University of Technology, Dalian, Liaoning, China. <sup>7</sup>Davidson School of Chemical Engineering, Purdue University, West Lafayette, IN, USA. <sup>8</sup>Institut de Physique et Chimie des Matériaux de Strasbourg (IPCMS), UMR 7504, CNRS - Université de Strasbourg, Strasbourg, France. <sup>9</sup>These authors contributed equally: Xiaoben Zhang, Shaobo Han, Beien Zhu, Guanghui Zhang. ✉e-mail: [gaoyi@zjlab.org.cn](mailto:gaoyi@zjlab.org.cn); [byang@dicp.ac.cn](mailto:byang@dicp.ac.cn); [gum@sustech.edu.cn](mailto:gum@sustech.edu.cn); [weiliu@dicp.ac.cn](mailto:weiliu@dicp.ac.cn)

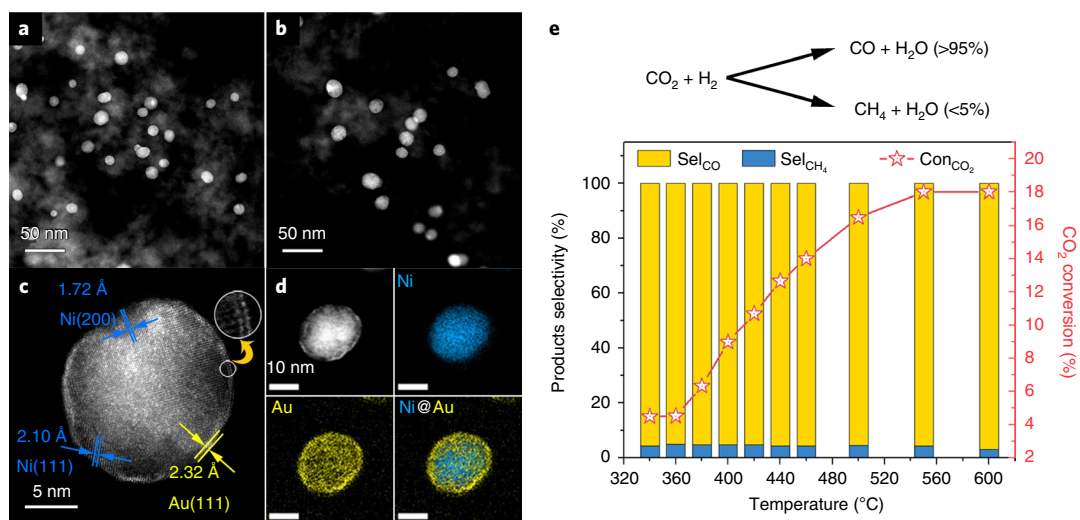


**Fig. 1 | Microstructure and catalytic performance of NiAu/SiO<sub>2</sub>.** **a, b**, HAADF images before **(a)** and after **(b)** the reaction. **c, d**, Atom-resolved HAADF image of one Ni@Au core-shell NP after the reaction **(c)** and energy dispersion spectroscopy analysis of its elemental distribution **(d)**. The NPs had a similar core-shell structure before the reaction (Supplementary Fig. 1). **e**, The catalytic performance of the Ni@Au/SiO<sub>2</sub> catalyst for CO<sub>2</sub> hydrogenation at atmospheric pressure (24 vol% CO<sub>2</sub> + 72 vol% H<sub>2</sub> + 4 vol% Ar at a space velocity of ~60,000 ml g<sub>cat</sub><sup>-1</sup> h<sup>-1</sup>). The microstructure and catalysis evaluation shows that the Ni@Au core-shell structure with an atomically ultrathin Au shell was maintained before and after the CO<sub>2</sub> hydrogenation and offered a continuous selectivity of 95% CO. Con, conversion; sel, selectivity.

ultrathin gold shell. Such an atomic thickness of the shell can be precisely interpreted based on an icosahedral encapsulation model under the Ni:Au ratio of 8:1 (Supplementary Fig. 2).

The catalytic performance of the Ni@Au/SiO<sub>2</sub> catalyst was tested for CO<sub>2</sub> hydrogenation. As displayed in Fig. 1e, the onset temperature of CO<sub>2</sub> hydrogenation was 340 °C with a conversion of ~4.5%, and the conversion increased to a maximum of about 18% at 600 °C. CO is the predominant product with a selectivity of 95% at all the reaction temperatures. The only other product was CH<sub>4</sub>, which suggests a preferred reaction path for the reverse water gas shift (CO<sub>2</sub> + H<sub>2</sub> = CO + H<sub>2</sub>O) over the methanation reaction (CO<sub>2</sub> + 4H<sub>2</sub> = CH<sub>4</sub> + 2H<sub>2</sub>O) on this catalyst. Based on ex situ STEM characterizations and the conventional understanding of core-shell nanocatalysts, one can easily assume that the ultrathin gold shell in NiAu bimetallic NPs catalysed the CO<sub>2</sub> hydrogenation for a highly selective CO production. However, despite the core-shell structure before and after the reaction, in situ STEM imaging (Supplementary Fig. 3) directly visualized a phase transition from the Ni@Au core-shell to a NiAu alloy at elevated reaction temperatures (200–500 °C), at which the core-shell structure does not contribute to the catalytic performance.

**Surface reconstruction dynamics during the reaction observed via in situ TEM.** An ETEM was employed for the in situ observation in the reaction atmosphere at near ambient pressure (9 ± 0.1 mbar, 25% CO<sub>2</sub>/75% H<sub>2</sub>). The large difference of atomic potentials between the Au and Ni atoms induces a remarkable modulation of the electron wave propagation<sup>18</sup>, which makes the Au rich atom columns appear darker and the Ni-rich ones brighter<sup>19,20</sup>. The simultaneously collected HAADF and bright-field images (Supplementary Fig. 4) on a NiAu NP offer a further intuitive illustration of such contrast characteristics. However, convincing imaging of the atomic Au shell using the TEM mode is challenging because the focus of the microscope inevitably changes due to the thermal vibration of the sample during the in situ reaction<sup>21</sup>. Therefore, a microscopy scripting method was developed to filter all 3,400 recorded images to obtain those with identical focusing conditions (Supplementary Information). Figure 2a displays the TEM images of one NiAu NP in a reaction environment heated from 450 to 600 °C and then cooled

to 400 °C, as indicated by the yellow arrows. At 450–500 °C, the ultrathin Au shell clearly appears as a dark edge around the NiAu NP. After increasing the temperature to 600 °C, the dark edge disappears, which suggests that the Au species at the outermost surface dissolve in the Ni matrix to form a mixed NiAu alloy. As the catalyst cooled to 450–400 °C, the darker Au edge reappeared, which indicates the recovery of the Ni@Au core shell structure. Supplementary Videos 1 and 2 provide more intuitive and kinetic insights into this reversible alloying/dealloying process. Reconstruction details at the NiAu surface were also monitored during the recovery process from the NiAu alloy to the Ni@Au core shell (Fig. 2b,c and Supplementary Fig. 5), which was validated by the microscopy simulation results (Supplementary Fig. 6). These demonstrate a fully alloyed state at 600 °C, at which the darker Au-rich columns were separately coordinated with Ni ones (Fig. 2b). The electron energy loss spectra from the central and edge points reveal identical states in terms of both peak position and L<sub>3</sub>/L<sub>2</sub> ratio, which suggests a good uniformity of the NiAu alloy surface. When cooled to 400 °C, one single Au atomic layer was identified to re-segregate epitaxially along the Ni(200) facet, but with either compressive or tensile strains. To minimize the influence of beam irradiation during the ETEM, we limited the in situ imaging to 400 °C and were only able to visualize the first-layer segregation of the Au shell, which still proved the reversibility of the alloying process in the Ni–Au system under a CO<sub>2</sub> hydrogenation reaction. To bridge the ‘pressure gap’ between the in situ ETEM experiments (~9 mbar) and the actual reaction conditions (1 bar)<sup>22,23</sup>, we carried out a control experiment using a gas-cell reactor, which allows simultaneous imaging under a 1 bar reaction environment (Supplementary Fig. 7), and we were able to reproduce the reaction-driven alloying of NiAu NPs, which confirmed the credibility of our original ETEM results.

**Phase evolution revealed via in situ electron diffraction.** In addition to real-space atomic-scale imaging for localized structure details, selected area electron diffraction (SAED) data were collected during the reaction from 300 to 500 °C to achieve a quantitative phase analysis via the overall statistics of spatial frequency on a large quantity of NiAu NPs (Fig. 2d and Supplementary Video 3). The evolution of diffraction peaks (intensities of integrated

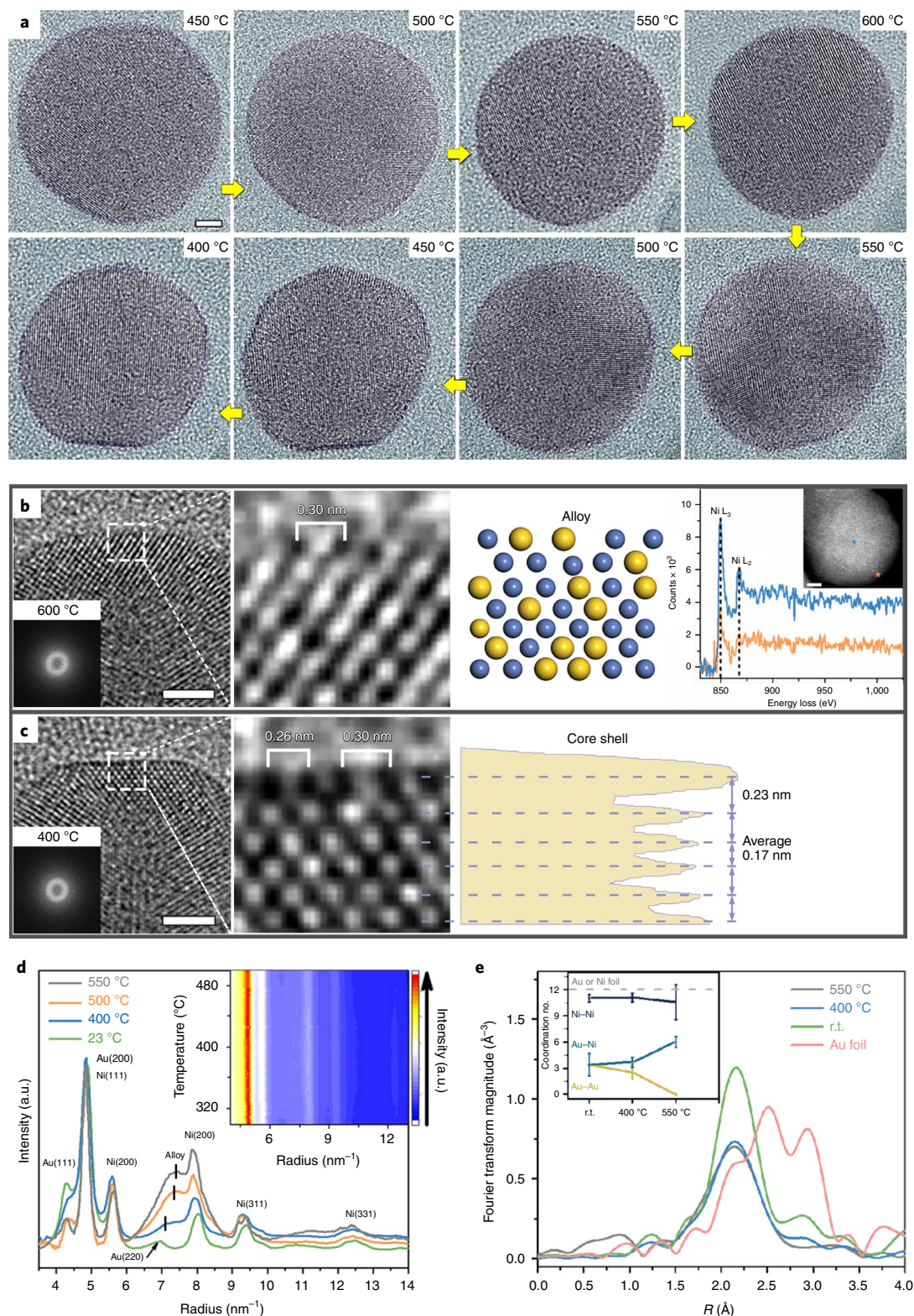


**Fig. 2 | In situ observation of the structural transition of NiAu NPs during the reaction.** **a**, In situ TEM imaging of the alloying and dealloying evolution of an individual NiAu particle during the  $\text{CO}_2$  hydrogenation reaction. Scale bar, 2 nm. **b, c**, Surface atom arrangement of a NiAu NP reconstructed from the full alloy (600 °C) (**b**) to the Ni@Au core-shell (400 °C) (**c**); the four parts from left to right in **b** show the high-resolution transmission electron microscopy (HRTEM) image (with a Thon ring inset), the corresponding enlargement of the surface area, schematic structure and point analysis of the electron energy loss spectra (with a HAADF inset); the three parts from left to right in **c** show the HRTEM image (with a Thon ring inset), the corresponding enlargement of the surface area and phase contrast profile. Scale bars, 2 nm. **d**, Intensity profiles from the integration of diffraction rings of selected area electron diffraction (SAED) patterns during the reaction. The inset shows 2D profiles stacking along with reaction temperature. **e**, In situ EXAFS of the Au  $L_3$  edge and coordination number changes (inset) of the Au-Au, Au-Ni and Ni-Ni pairs at room temperature (r.t.), 400 and 550 °C. The microstructural evolution during the catalytic reaction for the reconstruction from the Ni@Au core-shell to the NiAu alloy is evidenced through atomic scale microscopy (TEM/STEM and SAED) as well as the overall statistics of the spectroscopy (EXAFS and FTIR) (Supplementary Figs. 8 and 9). a.u., arbitrary units.

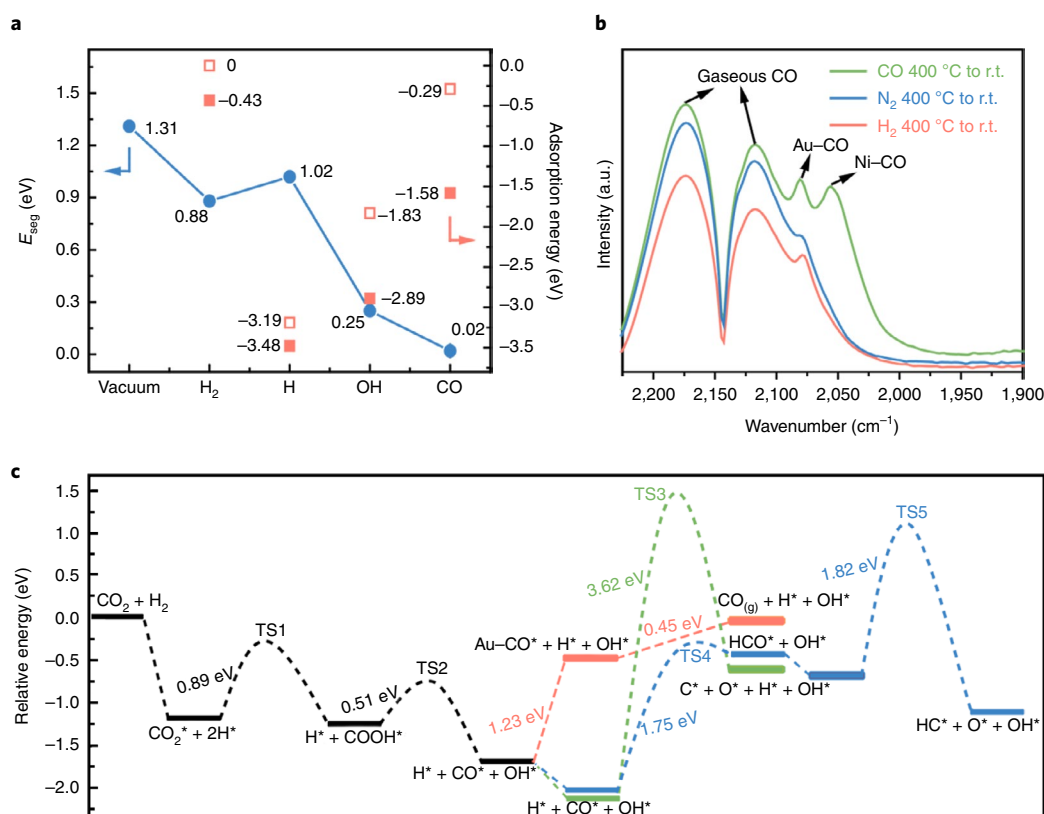


**Fig. 3 | Catalysis mechanism in the structural evolution of NiAu.** **a**,  $E_{\text{seg}}$  under the adsorption of  $\text{H}_2$ , H, CO and OH, and under vacuum (blue dots). Also shown are the adsorption energies of different adsorbates when all the Ni atoms are located in the bulk (hollow pink squares) and when a single Ni atom is moved to the Au surface (solid pink squares). **b**, FTIR spectra using CO as the probing molecule after fast quenching in  $\text{H}_2$ ,  $\text{N}_2$  and CO. **c**, The energy pathways of the  $\text{CO}_2$  hydrogenation reaction on the alloyed (111) surface of the  $\text{Ni}_3\text{Au}_1\text{-L}_{12}$  phase. The DFT calculation and FTIR reveal the mechanism of the alloying procedure and pathways of the reaction. TS, transition state.

diffraction rings) along with the temperature increase (Fig. 2d) discloses that a phase transition occurred at a temperature above  $400^\circ\text{C}$ , when a broadened diffraction peak that corresponds to the NiAu alloy phase emerged between the Au(220) and Ni(220) peaks. With a further increase in the reaction temperature, the diffraction of the alloy phase became stronger, whereas the diffraction from face-centred cubic Au-shell weakened. This behaviour confirms that the newly formed diffraction at a high temperature is from the alloyed NiAu phase. In addition, diffractions of the pure face-centred cubic Ni remained prominent after the Ni and Au were fully alloyed, which manifested that the alloying transition only involved the surface region and not the entire particle.

**Surface atom coordination analysed via in situ XAS.** We were able to confirm our microscopy observations of the structural transition of NiAu NPs using in situ XAS. The results of both the X-ray absorption near-edge spectroscopy (XANES) and extended X-ray absorption fine structure spectroscopy (EXAFS) are summarized in Supplementary Table 2. The Ni K-edge XANES spectra (Supplementary Fig. 8a) show a constant adsorption edge at  $8,333.0\text{ eV}$ , which evidences a Ni(0) metallic state under the reaction conditions<sup>24</sup>. As expected, only Ni neighbours at  $\sim 2.48\text{ \AA}$  were observed in the Ni K-edge EXAFS fitting results (Supplementary Fig. 8b), which is consistent with the high Ni/Au molar ratio ( $\sim 8$ ). The coordination number was always around 12 under all the reaction conditions, which validated the HAADF-STEM results by confirming that the majority of Ni component stayed in the bulk for particle sizes larger than  $10\text{ nm}$ . However, Au also maintained a similar electronic state under all the reaction

conditions (Supplementary Fig. 8c)<sup>25</sup>. Both the Ni and Au neighbours were observed in the Au  $L_3$ -edge EXAFS spectra at room temperature (r.t.). The EXAFS fitting results gave 3.4 Au neighbours at  $2.78\text{ \AA}$  together with 3.4 Ni neighbours at  $2.57\text{ \AA}$  (Fig. 2e). A total coordination number of 6.8 (much smaller than 12) suggests that most of the Au atoms were located on the surface (coordinately unsaturated). When the reaction temperature was increased to  $400^\circ\text{C}$ , an increase of the Au-Ni and a decrease of the Au-Au coordination number were observed, indicating a mixing of Au-Ni atoms and the surface Au atoms diffused into the Ni core (or vice versa), which is consistent with the ETEM observation (Fig. 2a). At  $550^\circ\text{C}$ , only Au-Ni scattering was observed at  $2.56\text{ \AA}$ , which suggests that all the Au atoms were surrounded by Ni neighbours at this temperature. The total coordination number for Au of  $\sim 6$  suggests that most of the Au atoms were still located on the outer surface.

**Surface structure evolution monitored via in situ FTIR spectroscopy.** To investigate the surface structure as well as the reaction intermediates (adsorbates), in situ FTIR experiments were performed in a flow gas mixture of  $2.5\% \text{ CO}_2/7.5\% \text{ H}_2/90\% \text{ He}$  (Supplementary Fig. 9). At  $30^\circ\text{C}$ , before the reaction initiated, no obvious adsorption was found. On heating to  $300^\circ\text{C}$ , a broad band of C=O stretching appeared at  $2,025\text{ cm}^{-1}$ , which can be assigned to the linear adsorption of CO intermediates on the surface Ni sites<sup>26,27</sup>. On increasing the temperature further to  $400^\circ\text{C}$ , the surface CO intermediates remained and additional gaseous CO was identified at  $\sim 2,175$  and  $\sim 2,113\text{ cm}^{-1}$  (ref. 28), which indicates the onset activity for  $\text{CO}_2$  hydrogenation. The results reveal the emergence of Ni species on the NiAu surface during the reaction, and demonstrate that

CO<sub>2</sub> activation yields CO as a surface intermediate and/or product in the temperature range 300–400 °C (Supplementary Fig. 9a). Further verification of the NiAu alloying process was explored using CO as a probing molecule<sup>29,30</sup>, as described in Supplementary Fig. 9b.

**Reaction-induced reconstruction mechanism analysed via DFT calculations.** The segregation energy ( $E_{\text{seg}}$ ) is defined as the energy required for a single Ni solute to move from the bulk to the surface Au layer<sup>31</sup>. We calculated  $E_{\text{seg}}$  with and without the adsorption of various reactants or intermediates during the CO<sub>2</sub> hydrogenation. The vacuum  $E_{\text{seg}}$  is 1.31 eV, which shows a strong Au surface-segregation trend and explains the stability of the initial Au shell both before the reaction and after the recovery of the Ni@Au core-shell structure. The adsorption of different species reduces the  $E_{\text{seg}}$  to different levels, as shown in Fig. 3a. In particular, the adsorption of CO causes the largest reduction such that  $E_{\text{seg}}$  is almost zero, which confirms that the increased Ni surface concentration was caused by the production of CO during the reaction. Further calculations of the segregation pathway showed that the CO adsorption may help to reduce the energy barriers that block the bulk Ni atoms from migrating to the surface, but its primary role is still to enhance the stability of the surface Ni atoms. (Supplementary Fig. 18). The CO-induced Ni surface segregation was further verified by quenching the NPs from 400 °C to r.t. in different gas environments which are able to ‘freeze’ the surface under high temperatures<sup>32,33</sup>. The CO FTIR spectra (Fig. 3b) reveal a preserved, Ni-rich NiAu alloy surface after quenching in CO, but only an Au-rich surface after quenching in either H<sub>2</sub> or N<sub>2</sub>. Besides, the absence of CO adsorption on Ni sites for the H<sub>2</sub> and N<sub>2</sub> quenched samples also implies that the segregated Au shell completely covers the Ni core for the Ni@Au core-shell. For completeness, we compared the performance of our Ni@Au catalyst with a specially designed homogeneous NiAu alloy with a 1:1 atomic composition for CO<sub>2</sub> hydrogenation. It turns out that both catalysts demonstrate a similar catalytic behaviour throughout the reaction, with related structural features, which further confirms the NiAu alloy as the active phase (Supplementary Figs. 19 and 20).

The re-segregated NiAu alloy surface was examined for reactivity and selectivity through the reaction-pathway calculations at the DFT level (Fig. 3c)<sup>34</sup>. The whole pathway can be divided into two stages. In the first stage, the CO<sub>2</sub> is hydrogenated at the Ni surface sites with the largest energy barrier of 0.89 eV. In the second stage, there are three possible pathways that lead to different final products. The direct dissociation of CO to form CH<sub>4</sub> has the largest energy barrier of 3.62 eV. The pathway to form CH<sub>4</sub> through a HCO intermediate, has two energy barriers of 1.75 eV and 1.82 eV. In the pathway that is the most energetically favoured the adsorbed CO molecules diffuse from the Ni site onto the Au site with an energy barrier of 1.23 eV and desorb there with an energy barrier of 0.45 eV. Therefore, we conclude that the surface Ni atoms offer the active sites for the hydrogenation of CO<sub>2</sub> and the surface Au atoms contribute for the selective production of CO.

## Conclusion

We report the in situ visualization of the dynamic surface alloying in Ni@Au core-shell NPs under CO<sub>2</sub> hydrogenation conditions, which cannot be resolved by ex situ characterizations either before or after the reaction. Our results call into question the general assumption that core-shell NPs maintain their configuration under working conditions, and indicate the need to re-examine the active phase of similar binary catalysts. Similar in situ catalytic studies and new design strategies based on in situ or operando feedback information are highly necessary.

## Methods

**Chemicals and materials.** Nickel(II) acetylacetonate (97.0%) and oleylamine (85.0%) were purchased from Aladdin Shanghai Co., Ltd; ammonium hydroxide

(NH<sub>3</sub>·H<sub>2</sub>O), chloroauric acid (HAuCl<sub>4</sub>·4H<sub>2</sub>O), acetone, *n*-hexane, ethanol and acetonitrile were purchased from Sinopharm Chemical Reagent Beijing Co., Ltd. Silica (surface area of 350–410 m<sup>2</sup> g<sup>-1</sup>) was purchased from Alfa Aesar. All the reagents were of analytical grade and used as-received without further purification.

**Sample preparation.** The NiAu NPs were synthesized by a typical wet chemical method reported elsewhere<sup>35</sup>. Briefly, 1.0 g of nickel(II) acetylacetonate was dissolved in 40 ml of oleylamine and then heated to 100 °C for 30 min to form a blue-green solution. Subsequently, a freshly prepared solution of HAuCl<sub>4</sub>·4H<sub>2</sub>O (0.2 g of HAuCl<sub>4</sub>·4H<sub>2</sub>O in 10 ml of ethanol) was added stepwise with vigorous stirring and then maintained at 120 °C for 60 min until the colour of the solution became dark purple. The solution was then heated to 230 °C within 10 min, and kept at 230 °C for 60 min before cooling down to r.t. Finally, the product was collected by centrifugation, washed with an acetone and hybrid solution (*n*-hexane and ethanol volume ratio of 3:1) in sequence and then redissolved in ethanol for further use. The fresh NiAu NPs were impregnated onto the silica with a total NiAu loading of 5 wt%, and then washed by CH<sub>3</sub>CN at 85 °C for 12 h to remove the surface organic absorbates. The collected powder was dried at 60 °C and served as the catalyst for further testing. The Au/SiO<sub>2</sub> samples used in the control experiments were prepared via a strong electrostatic adsorption method with a weight loading of ~1.5% (ref. 36). Briefly, 0.27 mmol HAuCl<sub>4</sub>·H<sub>2</sub>O was added into 250 ml of deionized water with the pH value adjusted to 11 by using NH<sub>3</sub>·H<sub>2</sub>O, and then mixed with 334 mg of SiO<sub>2</sub> by stirring for 1 h. The collected solid was reduced at 300 °C in H<sub>2</sub> in a tube furnace under a flow rate of 60–70 ml min<sup>-1</sup>. The morphology and surface adsorption properties are shown in Supplementary Fig. 10.

**Catalytic testing.** The catalytic testing was carried out in a U-tube fixed-bed reactor at ambient pressure. The catalyst was first reduced in pure H<sub>2</sub> (50 ml min<sup>-1</sup>) at 300 °C for 2 h with a ramp rate of 5 °C min<sup>-1</sup> from r.t. to 300 °C, before switching to a feed gas of 72 vol% H<sub>2</sub> + 24 vol% CO<sub>2</sub> + 4 vol% Ar (50 ml min<sup>-1</sup>). The reactivity was tested stepwise from 340 to 600 °C at 20 °C intervals, with a duration of 30 min at each temperature. Products were analysed online with an Agilent 7820 A gas chromatograph equipped with TDX-01 and a 5 Å molecular sieve column and PEG-20M capillary column. Gas products were examined with a thermal conductivity detector and a flame ionization detector. Conversion and selectivity were calculated according to equations (1)–(3):

$$\text{Conversion}_{\text{CO}_2} = \frac{\text{CO}_{2\text{inlet}} - \text{CO}_{2\text{outlet}}}{\text{CO}_{2\text{inlet}}} \times 100\% \quad (1)$$

$$\text{Selectivity}_{\text{CO}} = \frac{\text{CO}_{\text{outlet}}}{\text{CO}_{\text{outlet}} + \text{CH}_{4\text{outlet}} + \text{hydrocarbon}_{\text{outlet}}} \times 100\% \quad (2)$$

$$\text{Selectivity}_{\text{CH}_4} = \frac{\text{CH}_{4\text{outlet}}}{\text{CO}_{\text{outlet}} + \text{CH}_{4\text{outlet}} + \text{hydrocarbon}_{\text{outlet}}} \times 100\% \quad (3)$$

The selectivity of the hydrocarbon species was below 0.5%.

**Characterizations.** **STEM.** The atomic resolution microscopy analysis and elemental mapping were performed on a JEM ARM200F thermal-field emission microscope with a probe spherical aberration (Cs) corrector working at 200 kV. For the HAADF imaging, a convergence angle of ~23 mrad and a collection angle range of 68–174 mrad were adapted for the incoherent atomic number imaging. The elemental composition as well as distribution were studied on a microscope equipped with an energy dispersive X-ray analyser (EX-230 100 m<sup>2</sup> detector). For the STEM sample preparation, the two NiAu/SiO<sub>2</sub> catalysts before and after the reaction were dispersed in ethanol and dropped onto the copper grids and dried on a hot plate (150 °C).

In situ TEM experiments were carried out on the Titan Themis G3 ETEM (Thermo Scientific Company) in the electron microscopy centre at the Dalian Institute of Chemical Physics Chinese Academy of Sciences, which was used at 300 kV with a Cs corrector for parallel imaging (CEOS GmbH) and a measured resolution of better than 1.0 Å. The TEM images and video series were recorded by a Gatan OneView camera at a 4,096 × 4,096 pixel resolution under an exposure time of 0.5 s (two frames per second for the video recordings) at a dose rate of ~500 e Å<sup>-2</sup> s<sup>-1</sup>. During the in situ reaction of CO<sub>2</sub> hydrogenation, a mixer of CO<sub>2</sub> and H<sub>2</sub> in a volume ratio of 1 ± 0.1 to 3 ± 0.2 was generated using a mass flow controller and an inlet into the microscope that was differentially pumped at a stable octagon pressure (near the specimen) of 9 ± 0.1 mbar. The Ni–Au catalysts were loaded onto the chip of a MEMS (microelectromechanical systems)-based heating holder (FEI Nano-Ex) for the in situ reaction. A temperature ramping rate of 0.2 °C s<sup>-1</sup> for the thermal procedures at 500–600 °C (Supplementary Video 1 at a ×50 playback speed) and 600–400 °C (Supplementary Video 2 at a ×50 playback speed), and at a rate of 1 °C s<sup>-1</sup> for the in situ SAED at 300–500 °C (Supplementary Video 3 at a ×10 playback speed). The postanalysis of the TEM results was performed within the software package Digital Micrograph (GMS 3.22) as well as Image J (1.52a). In particular, given the parallel coherent imaging characteristic of the TEM method, to achieve a reliable judgement of the atomic layered Au shell based on the phase contrast sets a harsh requirement for the precise control of the focusing condition when performing the in situ imaging during the catalytic

reaction. Practically, in our experiments a focusing fluctuation was, indeed, inevitable due to the  $\text{Si}_3\text{N}_4$  supporting film transformation during the kinetic heating. Therefore, we adopted a postfiltering strategy to analyse the focusing condition of every TEM image for all the 3,400 recorded ones. Especially, a script was developed to extract the focusing condition based on calculating the Thon ring distribution of fast Fourier transform pattern, followed by filtering out those with identical defocusing values, which was within about a  $-5 \pm 1$  nm variation at a coherent contrast transfer range of about 1–3.3 Å (for a transfer intensity higher than 25%) to ensure the reliability of the phase contrast information.

In situ STEM analysis was utilized as complementary to the ETEM microscopy. HAADF imaging was primarily selected to maximize the collection of incoherent scattered electrons, which enabled us to collect images with a high contrast between different elements as the total detected intensity of the electron beam strongly depends on the atomic number of the specimen ( $I \propto Z^2$ ), in addition to its thickness. In particular, the in situ STEM analysis at a low reaction pressure (~2 Pa) was partially performed on a newly developed HF5000 microscope from the Hitachi Company with a 200 kV cold-field emission gun and a Cs-corrector for the electron probe. The kinetic STEM images were acquired under the HAADF mode at a collection angle range of 40–213 mrad with gas (pre-mixture of 25 vol%  $\text{CO}_2$  + 75 vol%  $\text{H}_2$ ) being inlet via a specially designed gas nozzle towards the sample location. The reaction was initiated via a MEMS-based heating method (using a MEMS compatible holder designed by Hitachi Company) with NiAu particles supported on the  $\text{Si}_3\text{N}_4$  membrane. For in situ STEM imaging at a reaction pressure of one atmosphere (1 bar), the experiments were performed with a JEOL 2100F microscope operating at 200 kV, equipped with a Cs corrector for the electron probe.

**FTIR spectroscopy.** All the in situ FTIR spectra were acquired in the transmission scanning mode in the range 1,000–4,000  $\text{cm}^{-1}$  at a 32-scan integral using a Bruker TENSOR27 spectrometer equipped with a mercury cadmium telluride detector, which facilitates a resolution of 4  $\text{cm}^{-1}$ . A cold trap with liquid nitrogen was used to exclude the possibility of  $\text{Ni}(\text{CO})_4$  contamination from the steel tube. By using a circulating water-cooling device, a quenching rate of 200  $^\circ\text{C min}^{-1}$  could be achieved from 500 to 300  $^\circ\text{C}$  and of 100  $^\circ\text{C min}^{-1}$  from 300 to 200  $^\circ\text{C}$ , effectively ‘freezing’ the surface structure at a high temperature as per our previous work<sup>33</sup>. The FTIR samples were made by pressing 7–13 mg of Ni@Au/SiO<sub>2</sub> or Au/SiO<sub>2</sub> into a wafer of diameter 13 mm.

During the in situ FTIR spectroscopy for the  $\text{CO}_2$  hydrogenation reaction, the NiAu samples were first reduced in 30  $\text{ml min}^{-1}$  flow of 15%  $\text{H}_2$  at 300  $^\circ\text{C}$  for 60 min, and then heated to 500  $^\circ\text{C}$  at the rate of 15  $^\circ\text{C min}^{-1}$  and kept at this temperature for 10 min before slowly cooling to r.t. The spectra were collected at 500, 400 and 300  $^\circ\text{C}$ , and then at r.t. (30  $^\circ\text{C}$ ) as the background. In situ  $\text{CO}_2$  +  $\text{H}_2$  FTIR experiments were then performed in a 2.5%  $\text{CO}_2$ /7.5%  $\text{H}_2$ /90% He mixture with a flow rate of 10–20  $\text{ml min}^{-1}$ . The spectrum was first acquired at r.t. Before heating to 300  $^\circ\text{C}$  (15  $^\circ\text{C min}^{-1}$ ) for acquisition, the NiAu sample was swept by 15%  $\text{H}_2$  to eliminate the surface adsorbates. The spectra were collected at 400 and 500  $^\circ\text{C}$  in the same way as for the hydrogenation reaction.

During the in situ FTIR spectroscopy for CO adsorption, CO was used as the probe molecule. The samples were first reduced in 30  $\text{ml min}^{-1}$  of 15%  $\text{H}_2$  at 300  $^\circ\text{C}$  for 60 min, and the background spectra were collected at 200, 300, 400 and 500  $^\circ\text{C}$ . Then a flow of 5% CO (10–20  $\text{ml min}^{-1}$ ) was used and the spectra collected at each temperature as the mixture slowly cooled (10  $^\circ\text{C min}^{-1}$ ) from 500  $^\circ\text{C}$  to r.t.

During the in situ FTIR spectroscopy for fast quenching in different atmospheres, a NiAu sample was first reduced in 30  $\text{ml min}^{-1}$  of 15%  $\text{H}_2$  at 300  $^\circ\text{C}$  for 60 min to collect the background spectrum when cooled to 30  $^\circ\text{C}$ . It was then heated in different gas environments ( $\text{CO}$ ,  $\text{H}_2$  or  $\text{N}_2$ ) to 400  $^\circ\text{C}$  and kept for 10 min before quenching to 30  $^\circ\text{C}$ . Then 5% CO (10–20  $\text{ml min}^{-1}$ ) was used for 10 min and the CO FTIR spectra collected at 30  $^\circ\text{C}$ .

**XAS.** The in situ X-ray absorption measurements were acquired on the bending magnet beam line of the Materials Research Collaborative Access Team (MRCAT) at the Advanced Photon Source, Argonne National Laboratory. Photon energies were selected using a water-cooled, double-crystal Si(111) monochromator, which was detuned by approximately 50% to reduce the harmonic reflections. Measurements were made in the transmission mode in a reaction gas with the components 3%  $\text{H}_2$  and 1%  $\text{CO}_2$ , balanced by helium at ambient pressure. Data points were acquired in three separate regions (energies relative to the elemental Ni K or Au L<sub>3</sub> edges): a pre-edge region (–250 to –30 eV, step size of 10 eV and dwell time of 0.25 s), the XANES region (–30 to +30 eV, step size of 0.5 eV and dwell time of 0.25 s) and the EXAFS region (to 13 Å<sup>–1</sup>, step size of 0.07 Å<sup>–1</sup>, dwell time of 1 s). The ionization chambers were optimized for the maximum current with a linear response (~10<sup>19</sup> photons detected per second) with 10% absorption in the incident ion chamber and 70% absorption in the transmission detector. A Ni or Au foil spectrum was acquired simultaneously with each measurement for energy calibration. Catalysts were treated in a continuous-flow reactor, which consisted of a quartz tube (1 inch (2.54 cm) outer diameter, 10 inch (25.4 cm) length) sealed with Kapton windows by two Ultra-Torr fittings. Ball valves were welded to each Ultra-Torr fitting and served as the gas inlet and outlet. An internal K-type thermocouple (Omega) was placed against the catalyst sample holder to monitor the temperature. Catalyst samples were pressed into a cylindrical sample holder, which consisted of

six wells, to form a self-supporting wafer. The catalysts were treated with a mixture of 3%  $\text{H}_2$  and 1%  $\text{CO}_2$  and balanced by helium at ambient pressure, and the data were collected under reaction conditions at r.t., 400 and 550  $^\circ\text{C}$ .

Standard procedures for the normalization and background subtraction were performed using the Demeter 0.9.25 software package. The edge energy of the XANES spectrum was determined from the inflection point in the leading edge, that is, the maximum in the first derivative of the leading edge of the XANES spectrum. The pre-edge energies were also obtained in the first derivative using the zero-crossing point. The coordination parameters were obtained by a least-squares fit in *R* space for the *k*<sup>2</sup>-weighted Fourier transformed data using Artemis.

**Theoretical calculations.** All the theoretical calculations were carried out via applying DFT. Details of these are presented in the Supplementary Discussion. The atomic coordinates of all the optimized computational models are deposited in the Cambridge Crystallographic Data Centre (CSD 1979031-1979068) and presented in the Supplementary Data Set.

**Online content.** Any methods, additional references, Nature Research reporting summaries, source data, extended data, supplementary information, acknowledgements, peer review information; details of author contributions and competing interests; and statements of data and code availability are available at <https://doi.org/10.1038/s41929-020-0440-2>.

## Data availability

All the data needed to support the plots and evaluate the conclusions within this article are present within it, the Supplementary Information or the Cambridge Crystallographic Data Centre (deposition no. CSD 1979031-1979068), or are available from the corresponding author upon reasonable request.

Received: 10 September 2019; Accepted: 10 February 2020;

Published online: 23 March 2020

## References

- Hansen, P. L. et al. Atom-resolved imaging of dynamic shape changes in supported copper nanocrystals. *Science* **295**, 2053–2055 (2002).
- Nolte, P. et al. Shape changes of supported Rh nanoparticles during oxidation and reduction cycles. *Science* **321**, 1654–1658 (2008).
- Yoshida, H. et al. Visualizing gas molecules interacting with supported nanoparticulate catalysts at reaction conditions. *Science* **335**, 317–319 (2012).
- Xin, H. L. et al. Revealing the atomic restructuring of Pt–Co nanoparticles. *Nano Lett.* **14**, 3203–3207 (2014).
- Wei, X. et al. Geometrical structure of the gold–iron(III) oxide interfacial perimeter for CO oxidation. *Angew. Chem. Int. Ed.* **57**, 11289–11293 (2018).
- Gawande, M. B. et al. Core–shell nanoparticles: synthesis and applications in catalysis and electrocatalysis. *Chem. Soc. Rev.* **44**, 7540–7590 (2015).
- Bhattarai, N., Casillas, G., Ponce, A. & Jose-Yacaman, M. Strain-release mechanisms in bimetallic core–shell nanoparticles as revealed by Cs-corrected STEM. *Surf. Sci.* **609**, 161–166 (2013).
- Bu, L. et al. Biaxially strained Pt/Pb/Pt core/shell nanoplate boosts oxygen reduction catalysis. *Science* **354**, 1410–1414 (2016).
- Tedsree, K. et al. Hydrogen production from formic acid decomposition at room temperature using a Ag–Pd core–shell nanocatalyst. *Nat. Nanotechnol.* **6**, 302–307 (2011).
- Tao, F. et al. Reaction-driven restructuring of Rh–Pd and Pt–Pd core–shell nanoparticles. *Science* **322**, 932–934 (2008).
- Zhan, W. C. et al. Crystal structural effect of AuCu alloy nanoparticles on catalytic CO oxidation. *J. Am. Chem. Soc.* **139**, 8846–8854 (2017).
- Chi, M. F. et al. Surface faceting and elemental diffusion behaviour at atomic scale for alloy nanoparticles during in situ annealing. *Nat. Commun.* **6**, 8925 (2015).
- Wang, F. et al. Tourmaline-modified FeMnTiO<sub>x</sub> catalysts for improved low-temperature NH<sub>3</sub>-SCR performance. *Environ. Sci. Technol.* **53**, 6989–6996 (2019).
- Vara, M. et al. Understanding the thermal stability of palladium–platinum core–shell nanocrystals by in situ transmission electron microscopy and density functional theory. *ACS Nano* **11**, 4571–4581 (2017).
- Wu, C. H. et al. Bimetallic synergy in cobalt–palladium nanocatalysts for CO oxidation. *Nat. Catal.* **2**, 78–85 (2019).
- Su, D. S., Zhang, B. & Schlögl, R. Electron microscopy of solid catalysts—transforming from a challenge to a toolbox. *Chem. Rev.* **115**, 2818–2882 (2015).
- Wang, D. & Li, Y. One-pot protocol for Au-based hybrid magnetic nanostructures via a noble-metal-induced reduction process. *J. Am. Chem. Soc.* **132**, 6280–6281 (2010).
- Duan, S., Wang, R. & Liu, J. Stability investigation of a high number density Pt/Fe<sub>2</sub>O<sub>3</sub> single-atom catalyst under different gas environments by HAADF-STEM. *Nanotechnology* **29**, 204002 (2018).
- Scherzer, O. The theoretical resolution limit of the electron microscope. *J. Appl. Phys.* **20**, 20–29 (1949).

20. Pennycook, S. J. & Boatner, L. A. Chemically sensitive structure-imaging with a scanning transmission electron microscope. *Nature* **336**, 565–567 (1988).
21. Williams, D. B. & Carter, C. B. (eds) *Transmission Electron Microscopy: A Textbook for Materials Science* 483–506 (Springer, 1996).
22. Hansen, T. W. & Wagner, J. B. Catalysts under controlled atmospheres in the transmission electron microscope. *ACS Catal.* **4**, 1673–1685 (2014).
23. Xin, H. L., Niu, K., Alsem, D. H. & Zheng, H. In situ TEM study of catalytic nanoparticle reactions in atmospheric pressure gas environment. *Microsc. Microanal.* **19**, 1558–1568 (2013).
24. Takenaka, S., Kobayashi, S., Ogihara, H. & Otsuka, K. Ni/SiO<sub>2</sub> catalyst effective for methane decomposition into hydrogen and carbon nanofiber. *J. Catal.* **217**, 79–87 (2003).
25. Liu, X. et al. Structural changes of Au–Cu bimetallic catalysts in CO oxidation: in situ XRD, EPR, XANES, and FT-IR characterizations. *J. Catal.* **278**, 288–296 (2011).
26. Ueckert, T., Lamber, R., Jaeger, N. I. & Schubert, U. Strong metal support interactions in a Ni/SiO<sub>2</sub> catalyst prepared via sol–gel synthesis. *Appl. Catal. A* **155**, 75–85 (1997).
27. Beniya, A., Isomura, N., Hirata, H. & Watanabe, Y. Low temperature adsorption and site-conversion process of CO on the Ni(111) surface. *Surf. Sci.* **606**, 1830–1836 (2012).
28. Lang, R. et al. Non defect-stabilized thermally stable single-atom catalyst. *Nat. Commun.* **10**, 234 (2019).
29. Yang, F., Yao, Y., Yan, Z., Min, H. & Goodman, D. W. Preparation and characterization of planar Ni–Au bimetallic model catalysts. *Appl. Surf. Sci.* **283**, 263–268 (2013).
30. Mihaylov, M., Knözinger, H., Hadjiivanov, K. & Gates, B. C. Characterization of the oxidation states of supported gold species by IR spectroscopy of adsorbed CO. *Chem. Ing. Tech.* **79**, 795–806 (2007).
31. Ruban, A. V., Skriver, H. L. & Nørskov, J. K. Surface segregation energies in transition-metal alloys. *Phys. Rev. B* **59**, 15990–16000 (1999).
32. Swiatkowska-Warkocka, Z., Pyatenko, A., Krok, F., Jany, B. R. & Marszalek, M. Synthesis of new metastable nanoalloys of immiscible metals with a pulse laser technique. *Sci. Rep.* **5**, 9849 (2015).
33. Liu, W., Sun, K. & Wang, R. In situ atom-resolved tracing of element diffusion in NiAu nanospindles. *Nanoscale* **5**, 5067–5072 (2013).
34. Porosoff, M. D., Yan, B. & Chen, J. G. Catalytic reduction of CO<sub>2</sub> by H<sub>2</sub> for synthesis of CO, methanol and hydrocarbons: challenges and opportunities. *Energ. Environ. Sci.* **9**, 62–73 (2016).
35. Duan, S. & Wang, R. Au/Ni<sub>12</sub>P<sub>5</sub> core/shell nanocrystals from bimetallic heterostructures: in situ synthesis, evolution and supercapacitor properties. *NPG Asia Mater.* **6**, e122 (2014).
36. Wong, A., Liu, Q., Griffin, S., Nicholls, A. & Regalbutto, J. R. Synthesis of ultrasmall, homogeneously alloyed, bimetallic nanoparticles on silica supports. *Science* **358**, 1427–1430 (2017).

## Acknowledgements

This work received financial support from Talents Innovation Project of Dalian (2016RD04), CAS Youth Innovation Promotion Association (2019190) and the Natural Science Foundation of China (21773287, 11604357, 21872145, 21902019, 11574340 and 51874115); G.Z. and J.T.M. were supported in part by the National Science Foundation under Cooperative Agreement no. EEC-1647722. G.Z. also acknowledges the Fundamental Research Funds for Central Universities (DUT18RC(3)057). B.Z. thanks the financial support of the Key Research Program of Frontier Sciences, CAS, Grant no. ZDBS-LY-7012. Use of the Advanced Photon Source was supported by the US Department of Energy, Office of Basic Energy Sciences, under contract no. DE-AC02-06CH11357. MRCAT operations, beamline 10-BM, are supported by the Department of Energy and the MRCAT member institutions; the computational resources utilized in this research were provided by the National Supercomputing Center in Guangzhou (NSCC-GZ), Tianjin and Shanghai. In situ TEM work was also supported by NSFC 21802065 and was partially conducted at the picocenter of SUSTech CRF that receives funding from the Shenzhen government. We especially acknowledge H. Matsumoto and C. Zeng from Hitachi High-Technologies Co., Ltd, for the in situ STEM characterization; S. Liu from Dalian Jiaotong University for the focusing filtering and alignment on HRTEM images via scripting. This work is dedicated to the late D. Su for his valuable support and discussions.

## Author contributions

The project was conceived by W.L. X.Z. performed the catalyst preparation, FTIR and partial TEM characterizations and data analysis under the supervision of W.L. S.H. and M.G. conducted part of the ETEM experiments and data analysis. B.Z., X.L. and Y.G. conducted the mechanism analysis via DFT calculations as well as the manuscript preparation. G.Z. and J.T.M. performed the in situ XAS measurements and structure analysis. Z.W. contributed to the catalyst preparation and reaction measurements. B.Y. performed part of the FTIR experiments and data analysis. Y.L., W.B. and O.E. conducted the in situ TEM experiment under atmospheric pressure.

## Competing interests

The authors declare no competing interests.

## Additional information

**Supplementary information** is available for this paper at <https://doi.org/10.1038/s41929-020-0440-2>.

**Correspondence and requests for materials** should be addressed to Y.G., B.Y., M.G. or W.L.

**Reprints and permissions information** is available at [www.nature.com/reprints](http://www.nature.com/reprints).

**Publisher's note** Springer Nature remains neutral with regard to jurisdictional claims in published maps and institutional affiliations.

© The Author(s), under exclusive licence to Springer Nature Limited 2020